Journal of Environmental & Earth Sciences
https://journals.bilpubgroup.com/index.php/jees

ARTICLE

Numerical Modelling of Tsunami Waves from Tonga Volcano on January 15, 2022

R. Kh Mazova [1*], ***Jorge Van Den Bosch F.*** [2], ***Gustavo Oses A.*** [2], ***Andrey Kurkin*** [13], ***Ivan Smirnov*** [1]

[1] *Nizhny Novgorod State Technical University n.a. R.E. Alekseev, Nizhny Novgorod 603155, Russia*
[2] *Engineering Center Mitigation Natural Catastrophes, Faculty of Engineering, University of Antofagasta, Antofagasta 1240000, Chile*
[3] *V.I. Il'ichev Pacific Oceanological Institute Far Eastern Branch Russian Academy of Sciences, Vladivostok 690041, Russia*

ABSTRACT

The paper considers a catastrophic event - the eruption of Hunga Tonga-Hunga Ha'apai volcano on January 15, 2022. The process of preparation and eruption of Hunga Tonga volcano generated tsunami waves that were observed throughout the World Ocean. This event was notable for its unprecedented global impact and the early appearance of tsunami waves at distant coastal stations. So, the first waves at tide gauge stations in Chile and Peru were recorded 4 hours earlier than the arrival time of tsunami waves to the tide gauge after the eruption of Tonga volcano. Two mechanisms are possible for the generation of early tsunami waves: acoustic Lamb waves generated by a volcanic explosion and submarine landslides that occurred on the slopes of the volcano during the preparatory phase of the eruption. In this study, numerical simulation of various pre-eruption landslide scenarios on the slope of Hunga Tonga volcano is carried out in an attempt to explain these early tsunami waves. Under computation the elastoplastic model of landslide was taken into account. Wave characteristics of a tsunami on the coast of Chile and Peru generated by a landslide process on a volcanic slope are obtained. A detailed comparison of virtual tide gauge data with observational ones is used to validate this model. The results obtained can be used to improve early warning systems.

Keywords: Volcanic Eruption; Landslide Process; Acoustic and Tsunami Waves; Numerical Simulation; Tsunami Wave Characteristics

*CORRESPONDING AUTHOR:
R. Kh Mazova, Nizhny Novgorod State Technical University n.a. R.E. Alekseev, Nizhny Novgorod 603155, Russia; Email: raissamazova@yandex.ru

ARTICLE INFO
Received: 10 November 2024 | Revised: 30 November 2024 | Accepted: 6 December 2024 | Published Online: 17 January 2025
DOI: https://doi.org/10.30564/jees.v7i2.7686

CITATION
Mazova, R.K., Van Den Bosch F., J., Oses A., G., et al., 2025. Numerical Modelling of Tsunami Waves from Tonga Volcano on January 15, 2022. Journal of Environmental & Earth Sciences. 7(2): 13–30. DOI: https://doi.org/10.30564/jees.v7i2.7686

1. Introduction

Underwater earthquakes are the primary cause of tsunami waves, though tsunamis can also result from landslides, meteorological events, and volcanic eruptions[1]. Volcanic tsunamis, which originate from volcanic activity, can be triggered by several mechanisms, including volcano-tectonic earthquakes, underwater landslides, atmospheric acoustic waves, and caldera collapse[2]. This paper focuses on one of the largest volcanic tsunamis in recorded history, generated by the eruption of the Hunga Tonga volcano in January 2022.

On January 15, 2022, at 4:15 (UT), a major eruption occurred at the Hunga Tonga-Hunga Ha'apai volcano. Located within the Kingdom of Tonga, an island nation in the southwestern Pacific Ocean, Hunga Tonga-Hunga Ha'apai is one of several active underwater volcanoes in the region (**Figures 1** and **2**)[3]. Geographically, the volcano lies over 3,200 km northeast of Australia, 700 km south of Samoa, 500 km west of Niue, and 600 km east of Fiji. Its coordinates are S. 20º32′42″ and W. 175º23′33″[4]. The eruption was accompanied by an enormous explosion, registering a 5 on the Volcanic Explosivity Index (VEI)[5]. At its maximum extent, the volcanic plume reached a diameter exceeding 650 km. The estimated energy release from the explosion was equivalent to 200 megatons of TNT. The force of the explosion triggered a magnitude 5.8 earthquake[4], and the sound of the explosion was reportedly heard as far away as Alaska[6].

Hunga Tonga is an active stratovolcano, formed by the westward subduction of the Pacific tectonic plate beneath the Australian Plate along the Tonga-Kermadec Trench. This trench is an oceanic feature extending between Samoa and New Zealand in the southwest Pacific Ocean[3].

Figure 1. Location of Tonga Volcano.

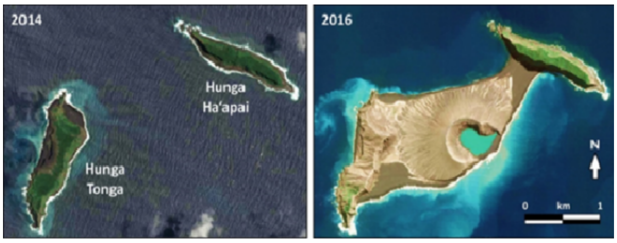

(**a**) (**b**)

Figure 2. Formation of the volcano cone by sediment from the 2014/15 eruptions. **a**) image of the volcano in 2014; **b**) right in 2016.

However, the eruptions prior to January 15, 2022, are not comparable to the one that occurred on this date, which resulted in the separation of the Hunga-Tonga and Hunga-Ha'apai islands once again[7–9]. The volcanic explosion triggered a multitude of geophysical processes, but of particular interest to this study is the formation of acoustic-gravity waves and tsunami waves. The explosive nature of the eruption, accompanied by powerful atmospheric disturbances, led to significant variations in air pressure over vast distances due to the propagation of atmospheric-acoustic waves (Lamb waves), which impact on the ocean is similar to interactions between atmospheric circulation and sea level (cf/ with[10]) The explosion generated three direct and three reflected Lamb waves that circled the globe[4].

A notable feature of this eruption was the subsequent tsunami, whose waves were recorded around the world. It was observed that the first wave was the largest. According to a resident of the capital of the Kingdom of Tonga, a series of explosions was heard first, and approximately 15 minutes later, the first tsunami wave was recorded. In total, three large waves impacted the coast of Tonga[11]. The Tongan government reported that the largest waves, reaching heights of up to 15 meters, struck the west coast of Tongatapu, as well as the islands of Eua and parts of the Ha'apai group[3].

Remarkably, comparable or even higher wave heights were observed in distant regions. Sea level oscillations were recorded not only across the Pacific Ocean but also in the Atlantic and Indian Oceans[8]. The tsunami waves generated by the January 15, 2022 eruption are comparable to those caused by the Krakatoa eruption in 1883. However, unlike the Krakatoa event, the waves from the Tonga eruption were recorded globally by modern tools (**Figure 3**), greatly facilitating the analysis of the event (see, also **Table 1**).

Table 1. Data on tsunami wave heights from the Tonga volcanic eruption.

Observation Point	Wave Height (m)	Observation Point	Wave Height (m)
Nuku'alofa (Kingdom of Tonga)	1.5–2	Kagoshima (Japan)	1.2
Hawaii (USA)	0.82	Tosashimizu (Japan)	0.9
Port San Luis (USA, CA)	1.3	Chichi-jima (Japan)	0.9
Arena Cove (USA, CA)	1.1	Tohoku (Japan)	0.7
South Coast of Oregon (USA)	more 0.3	Iwate (Japan)	1.1
New Zealand	more 1	Vodopadnaya Station (Russia, Kuril Islands)	1.4
Samoa (USA)	0.6	Guerrero, Colima, Baja California (Mexico)	0.61
Vanuatu	1–2.5	Manzanillo (Mexico)	2.05
Norfolk Island (Australia)	1.27	Zihuatanejo (Mexico)	1.19
Lord Howe Island (Australia)	1.10	Arica (Chile)	1.18
Gold Coast (Australia)	0.82	Coquimbo (Chile)	1.43
State of New South Wales (Australia)	0.5		

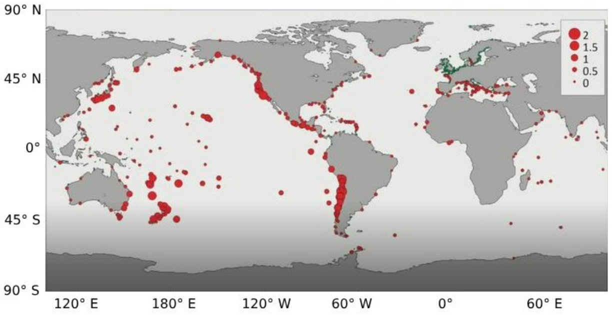

Figure 3. Data on tsunami wave heights from the Tonga volcanic eruption[8, 10].

2. Analysis of Acoustic and Marine Gravity Wave Data from the Tonga Volcanic Eruption

The Tonga volcanic tsunami is notable for being recorded on a global scale, with higher propagation velocities, unexpected far-field wave heights, and an unprecedented duration compared to tsunamis generated by seismic activity[8]. In fact, the tsunami arrived at global stations much earlier than expected from a typical tsunami generated in the Hunga Tonga–Hunga Ha'apai volcano region. A comparison of the travel times between the possible tsunami generated by the volcanic explosion and the observed tsunami reveals that the latter traveled 2.5 to 5 times faster, crossing the Pacific, Atlantic, and Indian Oceans in less than 20 hours.

This discrepancy in propagation speed is particularly evident in the far-field regions. For instance, the tsunami reached the coast of Japan and Chile in under 7 and 10 hours, respectively, whereas the expected travel time for a tsunami generated by the explosion would have been 10.5 to 12.5 hours for Japan and 12 to 17 hours for Chile. In the Atlantic and Indian Oceans, the tsunami arrived even sooner. It reached the Caribbean in 10–11 hours, while waves generated by the explosion would have taken more than 26 hours to travel from the source area, around the South American continent, to the Caribbean. The same pattern was observed on the eastern coasts of the Atlantic and the Mediterranean Sea, where disturbances in the ocean were recorded after 16.5 hours in Portugal and 17.5 hours in Italy, compared to an expected arrival time of 27 and 32 hours, respectively[8].

Furthermore, it is hypothesized that the resulting tsunami waves may have been generated by two mechanisms: either by Lamb waves produced by the volcanic eruption or by underwater landslides on the volcano's slope, formed during the eruption's preparation phase. To test the hypothesis regarding the relationship between acoustic-gravity Lamb waves, which were generated by the explosion and travel at a known speed of 306–312 m/s[4], and the tsunami waves that were the first to arrive at the stations, the arrival times of the acoustic waves and the sea waves (possibly generated by the Lamb wave) were calculated. Additionally, the arrival times of long ocean waves, assuming they were generated at the moment of the explosion, were calculated using the formula for the speed of long ocean waves[8]. The wave speed is calculated as a function of gravity and the ocean depth along the path from the volcano to the target station.

To facilitate this calculation, a Python function was developed[12]. This function takes as input the bathymetric data of the study area, obtained from the GEBCO general bathymetric map of the oceans, the geographic coordinates of the wave source (the Tonga Volcano), and the coastal station, as well as the number of points along the route between the source and the station, which determines the calculation accuracy. The function calculates and returns the average depth of the points along the orthodrome, the shortest route between two points on the globe.

The data on water level oscillations at tidal stations in Peru (**Figure 4**), are presented in **Figures 5–13**. The tide gauge records presented in **Figures 5**, **7**, **9**, **11**, **13** were obtained from Chilean colleagues—Jorge Van Den Bosch Fernández, director of the Centro de Ingeniería para la Mitigación de Catástrofes Naturales, Facultad de Ingeniería (CIMCN), Universidad de Antofagasta, Antofagasta, Chile (**Figure 7**), and Mauricio Fuentes, Departamento de Geofísica, Universidad de Chile, Santiago, Chile (**Figures 7**, **9**, **11**, **13**) — contain Chile (**Figure 6**), New Zealand (**Figure 8**), Japan (**Figure 10**), and the USA (**Figure 12**).

Figure 4. Location of Callao station, Peru. The station is marked with a red.

Figure 5 presents a tide gauge record from the Callao station in Peru (**Figure 4**) for January 15, 2022, provided by CIMCN, University of Antofagasta, Chile. The green line marks the moment of the volcanic explosion, the gray line represents the estimated arrival time of sea waves, possibly generated by the Lamb acoustic wave, and the blue line indicates the arrival time of the tsunami waves at the station. (cf. with[13, 14]).

According to the record in **Figure 5**, the first waves reached the coast of Callao, Peru, 9 hours after the eruption. The tide gauge records from stations along the coast of Chile (**Figure 6**) for January 15, 2022 (provided by CIMCN, University of Chile) are presented in **Figure 7.** The green (left) line marks the moment of the volcanic explosion, the gray (middle) line represents the estimated arrival time of sea waves, possibly generated by the Lamb acoustic wave, and the blue (right) line indicates the arrival time of the tsunami waves at the stations. The stations are as follows: 2) Iquique, 3) Mejillones, 4) Antofagasta, 6) Caldera, 7) Coquimbo.

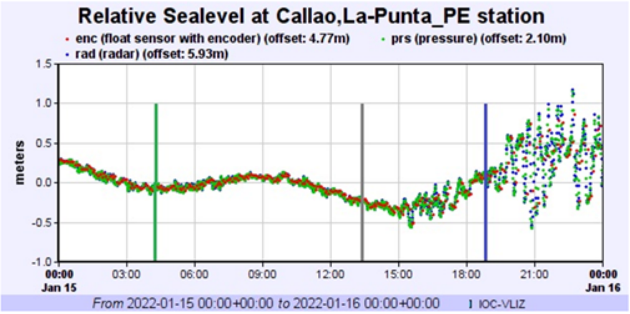

Figure 5. Record from the tide gauge at Callao station, Peru, for 15 January 2022.

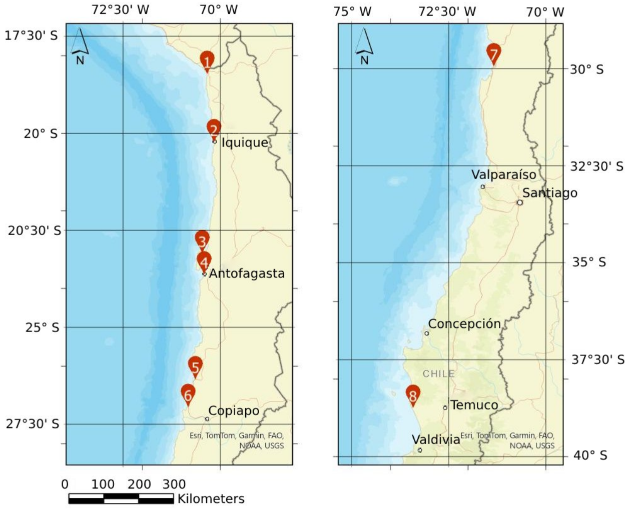

Figure 6. Location of stations on the coast of Chile. Stations are marked with red mark and numbered. 1—Arica; 2—Iquique; 3—Mejillones; 4—Antofagasta; 5—Chañaral; 6—Caldera; 7—Coquimbo; 8—Nehuentué.

Figure 8 presents tide gauge records from stations along the coast of Chile (**Figure 6**) for January 15, 2022, provided by the Department of Physics, University of Chile. The countdown begins at the moment of the volcanic explosion (green (left) line). The vertical gray (middle) line corresponds to the time of arrival of sea waves, possibly caused by the Lamb acoustic wave, to the tide gauge, the vertical blue (right) line indicates the time of arrival of tsunami waves to the tide gauge. The stations are as follows: 1) Arica, 4) Antofagasta, 5) Chañaral, 7) Coquimbo, and 8) Nehuentu.

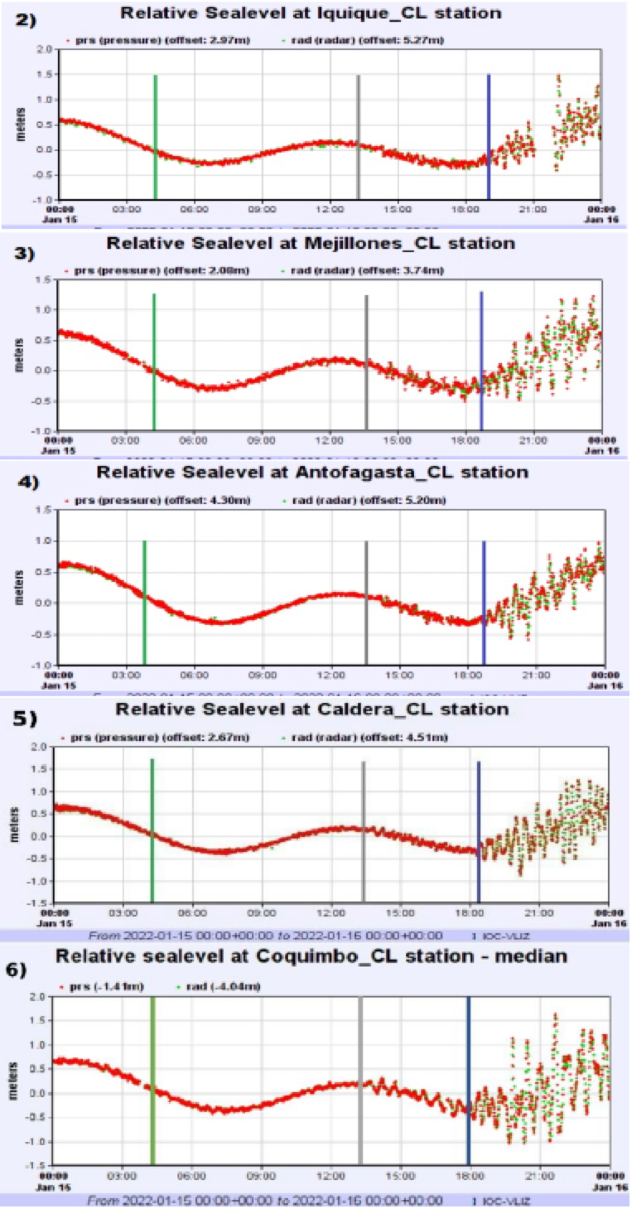

Figure 7. Records from Chilean coastal tide gauges for 15 January 2022 obtained from CIMCN, University of Antofagasta, Chile.

Unlike the records in **Figure 7**, the wave displacements caused by the volcanic eruption are more pronounced in **Figure 8**. Both **Figures 7** and **8** clearly show that the first waves reached the coast of Chile approximately 9 hours after the volcanic eruption. The maximum wave height was recorded at the Chañaral station (point 5 in **Figure 6**), reaching over 1.5 meters.

The following figures present tide gauge records for January 15, 2022, from other Pacific regions: New Zealand (southwestern Pacific Ocean, **Figures 9** and **10**), Japan (northwestern Pacific Ocean, **Figures 11** and **12**), and the USA (northeastern Pacific Ocean, **Figures 13** and **14**). These records were also obtained from the Department of Physics, University of Chile. The countdown in these recordings corresponds to the moment of the volcanic explosion, with the gray line indicating the estimated arrival time of sea waves, possibly caused by an acoustic Lamb wave, and the blue line showing the arrival time of the tsunami waves at each station.

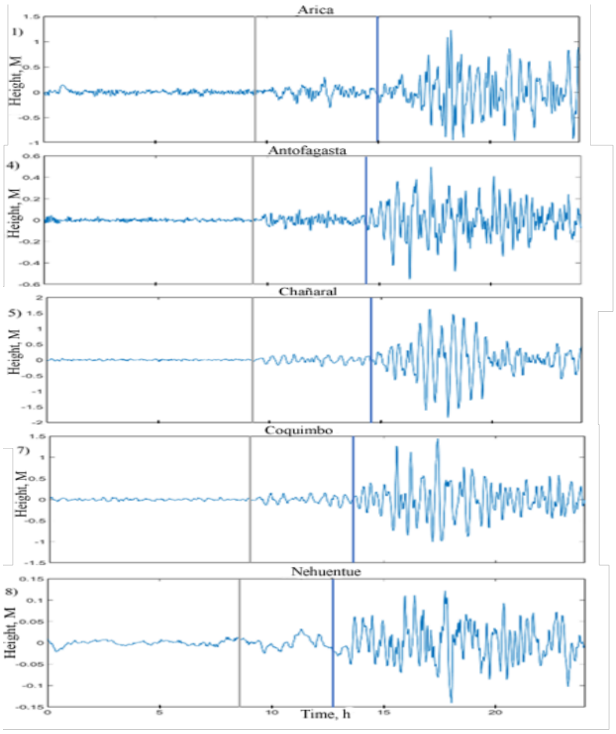

Figure 8. Records from the Chilean coast tide gauges for 15 January 2022 obtained from the Department of Physics, University of Chile[15].

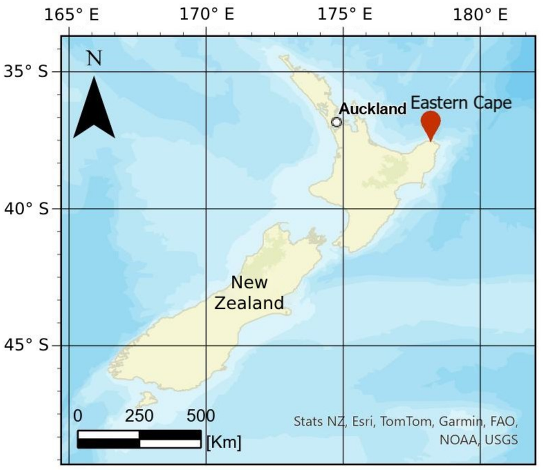

Figure 9. Location of the Eastern Cape station, New Zealand. The station is highlighted with a red mark.

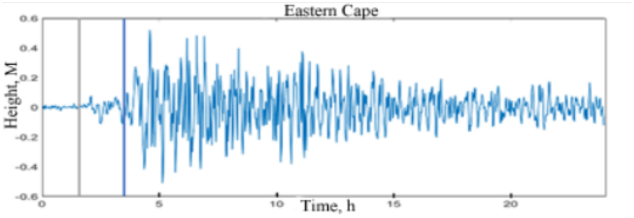

Figure 10. Record from the tide gauge at the Eastern Cape station, New Zealand, for 15 January 2022.

Figure 10 clearly shows that the first waves approached the Eastern Cape station in New Zealand 1.5 hours after the eruption and were up to half a meter high.

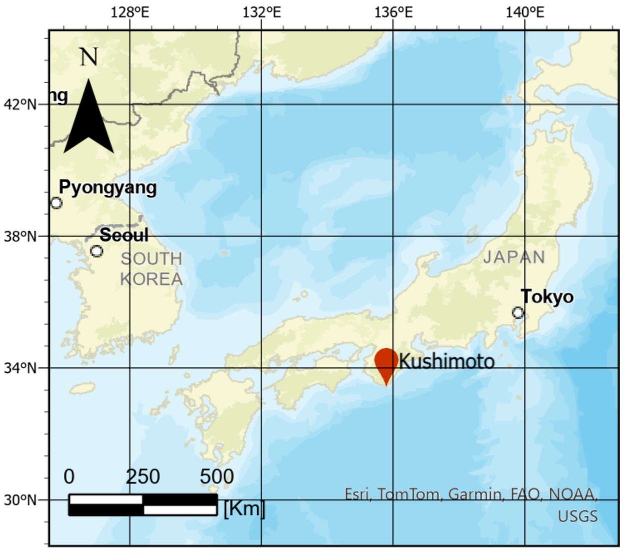

Figure 11. Location of Kushimoto station, Japan. The station is highlighted with a red mark.

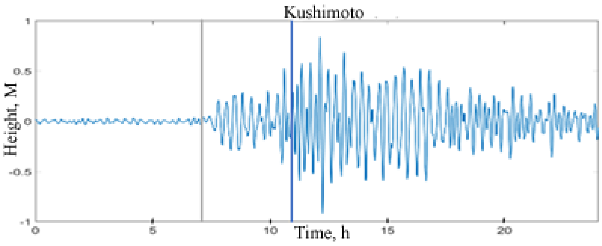

Figure 12. Record from the tide gauge at Kushimoto station, Japan, for 15 January 2022.

According to the entry in **Figure 12**, the first waves approached Kushimoto station in Japan 7 hours after the eruption and had a height of up to 0.8 m.

According to the record in **Figure 14**, the first waves reached the Los Angeles station in the USA 7.5 hours after the eruption, with a height of up to 0.4 meters. All these records show sea level oscillations, indicating that the Tongan volcanic tsunami was detected throughout the Pacific Ocean. The following **Table 2** presents the calculated characteristics of the waves, possibly caused by the eruption of the Hunga Tonga volcano, for each station.

Figure 13. Location of the Los Angeles station, USA. The station is highlighted with a red mark.

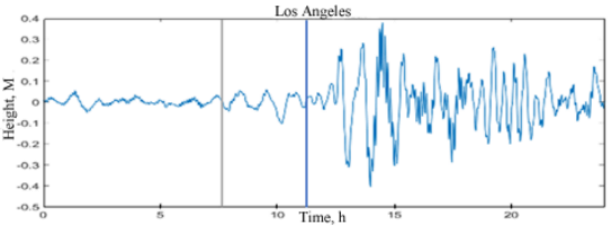

Figure 14. Record from the tide gauge at Los Angeles station, USA, for 15 January 2022.

In all tide gauge records, a noticeable correlation can be observed between the first waves recorded at the stations and the calculated waves presumably generated by acoustic Lamb waves. It is also evident from the records that, after the arrival of the initial weak waves, stronger waves appear in the tide gauge records. The arrival time of these stronger waves coincides with the calculated arrival time of long gravitational waves, which suggests that long gravitational waves were generated at the moment of the explosion.

Furthermore, the resulting tsunami waves may have been produced by the combined influence of two mechanisms: a caldera collapse and underwater landslides. The possibility of a landslide-induced tsunami during the preparation of a volcanic eruption is a plausible explanation for

Table 2. Results of the calculation of the long gravity tsunami wave approach and waves possibly caused by an acoustic Lamb wave.

Points	Distance of Tide Gauge to Volcano, km	Average Distance Depth, m	Average Long Wave Velocity along Path km/h	Arrival Time for Tsunami Wave h:m	Arrival Time for Sea Waves
Antofagasta	10522	4175	729	14:27	9:33
Arica	10770	4093	721	14:56	9:32
Chañaral	10375	4218	732	14:10	9:11
Nehuentué	9571	4435	751	12:45	8:28
Coquimbo	10145	4316	741	13:42	8:58
Caldera	10324	4232	734	14:05	9:08
Mejillones	10544	4143	726	14:32	9:20
Iquique	10707	4123	724	14:47	9:28
Callao	10373	4184	729	14:13	9:11
Eastern Cape	1746	1746	502	03:29	1:33
Kushimoto	7932	4131	725	10:57	7:01
Los Angeles	8543	4629	767	11:08	7:33

the appearance of tide gauge records before the arrival of a tsunami wave following a volcanic eruption. To test the hypothesis of a landslide-generated tsunami, we will assess the likelihood of an underwater landslide occurring during the preparation phase to the eruption.

The volcano is located near the deep Tonga-Kermadec Trench (**Figure 15**), which has a steep slope descending to a depth of up to 10,800 meters. This depression was formed by the westward subduction of the Pacific tectonic plate beneath the Australian plate[3].

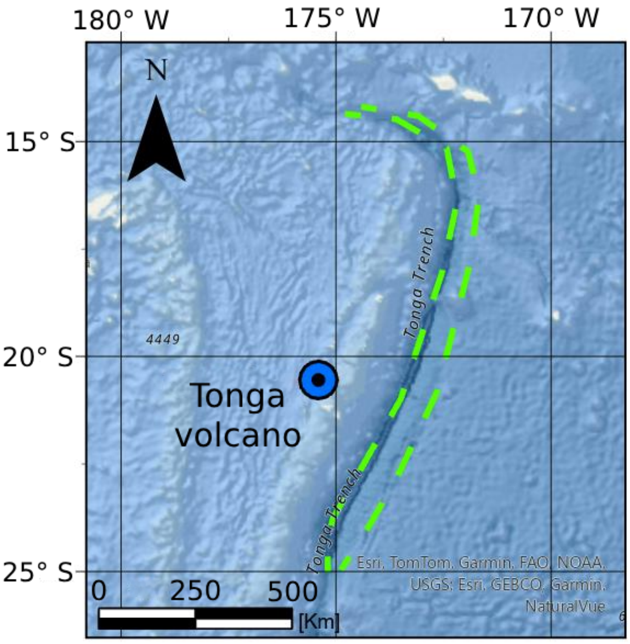

Figure 15. Tonga-Kermadec deep-sea trench. The trench is highlighted with a green dotted line. Tonga volcano is the blue dot.

3. Possible Landslide Mechanism for Tsunami Generation in Preparation of a Volcanic Eruption

To assess the possible localization of a landslide on a slope, cross sections of the northwestern part transverse sections of the volcano were made (**Figure 16**) and the dimensions of a possible landslide were determined (see below). Sections were made using the Profile tool, a version of Surfer software designed for surface analysis and modeling.

The data obtained suggest complex geophysical processes accompanying the powerful eruption of the Hunga-Tonga–Hunga-Ha'apai volcano on January 15, 2022. The observed wave processes in the coastal zone can be interpreted as the result of various physical phenomena during the preparation and eruption of the Hunga-Tonga–Hunga-Ha'apai volcano, such as the generation of a tsunami by

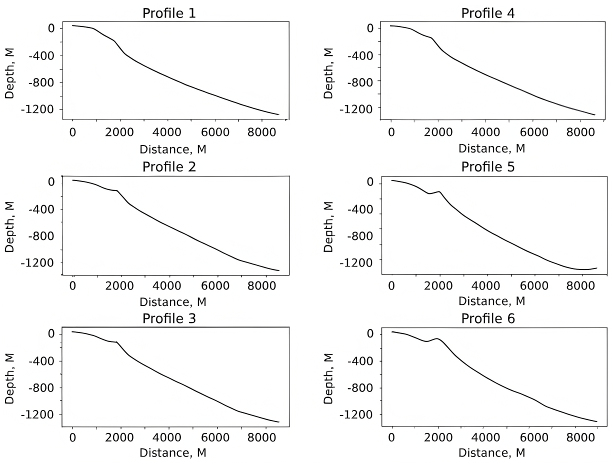

Figure 16. *Cont.*

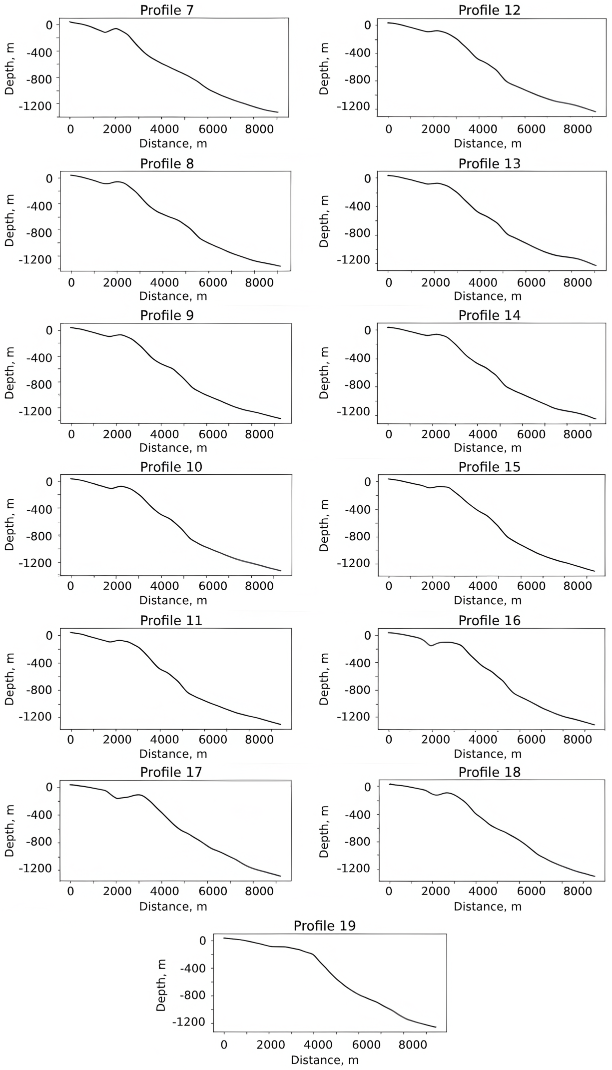

Figure 16. Regular cross-sections of the northwestern part of the Honga-Tonga volcano (sections 1–19) in the direction of the west coast of Chile.

an acoustic wave or a landslide on the volcanic slope during the eruption's preparatory phase.

4. Problem Statement

Landslide bodies are typically formed on the slopes of underwater features, which often have steep inclines. Volcanic or seismic activity can also cause part of the slope to slide, potentially generating a surface long wave (tsunami). Most models of landslide-generated tsunamis are based on the sea surface's response to the movement of the solid seabed. Various models describe the movement of landslide masses, such as the rigid body model[16, 17], the visco-plastic fluid model (see, e.g.,[18, 19]), and some others[20–22]. In the elastic-plastic fluid model[23–27]. the landslide begins to move when a yield stress value is reached (see **Figure 17** for the maximum critical value.).

The trigger for this movement could be either an earthquake or the preparatory phase of a volcanic eruption, which "pushes" the landslide mass down the slope, leading to its displacement. The elastic-plastic model provides the most accurate values for simulating the deformation of real grounds (see, for example,[23]).

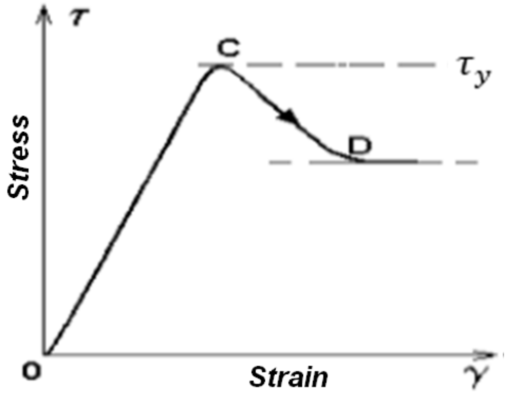

Figure 17. Model rheology of the landslide body: stress-strain dependence for elastic-plastic model of a landslide body (for details, see e.g.,[23]).

However, it is important to consider the rheological properties of the landslide, such as density, cohesion, tensile strength, and several other factors, for which information is currently lacking for the soils on the volcano's slopes. Therefore, based on the available information on the types of landslides mentioned above, we modeled the landslide process as a rigid body composed of multiple segmental blocks. The landslide was simulated by the dynamic vertical displacement of these segmental blocks along the slope, representing the sliding of the landslide mass[23]. The kinematics of block movement is determined by the schematic behavior of the landslide, consistent with the typical implementation of the elastic-plastic model—where the upper part of the landslide layer slides while the thickness of the lower part of the slope increases simultaneously (**Figure 18**; see also[23–26]).

Figure 18 presents a schematic of the sliding process of a landslide body along an underwater slope. This sliding can be approximated by the downward displacement of the upper segment blocks and the corresponding upward displacement of the lower blocks. For example, the height of the first block on the left decreases to zero, while the 8th block on the right rises to the same height that the first block originally had. Block 2 then moves to zero, and block 9 on the right reaches the initial height of block 2, and so on. Each reverse movement takes 20 seconds.

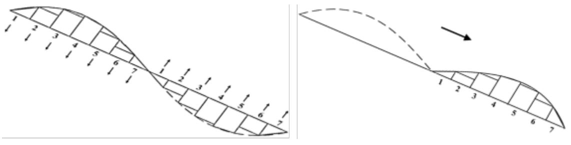

(**a**) (**b**)

Figure 18. Schematic representation of landslide body localization on the submarine slope Scenario 1: **a**) sequential segment displacement; **b**) Final position of the landslide body.

For a large landslide, the movement of segmental blocks shown in **Figure 19a,b** will occur in 4 stages. The time of segmental movement is different, each taking a different amount of time, but is selected so that the envelope of segmental displacement reflects the dynamics similar to the elastic-plastic variant of the process. The final position of the landslide body is shown in Figure 19b. The difference between Scenario 3 and Scenarios 1 and 2 (**Figure 19c**) is that although the process of landslide mass movement along the slope also occurs in 4 stages, but at each stage the displacement of segments occurs simultaneously, and each stage of displacement takes a finite time, e.g. 10 or 20 sec. As can be seen from the schematic representation in **Figure 19**, each decrease in the landslide thickness corresponds to a simultaneous increase in the thickness of the lower part of the slope.

The yield stress τ_y, at which the landslide begins to move could have been triggered by either minor seismic forshocks, of which there were many before the eruption, or the process of eruption preparation itself, during which stress gradually accumulated until it reached the critical limit, leading to the volcanic eruption. Therefore, the exact moment when the critical stress was reached can only be determined by solving the inverse problem, based on the arrival time of the first wave train at a specific coastline.

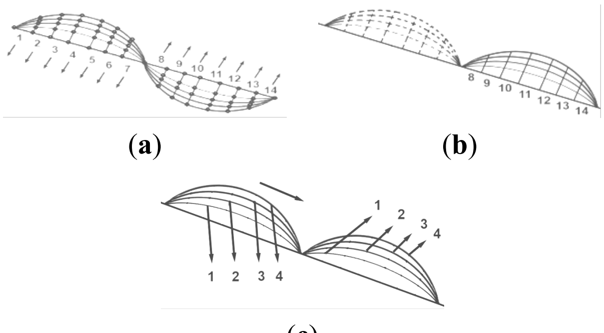

(**c**)

Figure 19. Schematic representation of landslide body displacement along the underwater slope: **a**,**b**) Scenario 2 (sequential displacement of blocks); **c**) Scenario 3 (simultaneous displacement of segments - 4 steps).

5. Mathematical Formulation of the Problem

To describe the generation and propagation of a wave by an underwater landslide (**Figure 19**), shallow water equations will be used in the following form[23–28], where *x*, *y* are the spatial coordinates along the Ox and Oy axes, respectively, *t* is the time, is the disturbance of the free surface relative to its undisturbed level, *g* is the acceleration due to ngravity, *h* is the maximum depth of the basin, *u(x, y, t)*, *v(x, y, t)* are velocity components along the Ox and Oy axes, The value *D*(*x*,*y*,*t*) determines the change in the thickness of the landslide during the sliding process (**Figures 17–19**), *r* is the coefficient of bottom friction, *f* is the Coriolis force

$$\frac{\partial u}{\partial t}+u\frac{\partial u}{\partial x}+\nu\frac{\partial u}{\partial y}+g\frac{\partial \eta}{\partial x}=fu-\frac{r}{h}u\sqrt{u^2+\nu^2} \tag{1}$$

$$\frac{\partial \nu}{\partial t}+u\frac{\partial \nu}{\partial x}+\nu\frac{\partial \nu}{\partial y}+g\frac{\partial \eta}{\partial y}=f\nu-\frac{r}{h}u\sqrt{u^2+\nu^2} \tag{2}$$

$$\frac{\partial \eta}{\partial t}=\frac{\partial D}{\partial t}-\frac{\partial h_s}{\partial t}-\frac{\partial}{\partial x}\left(\left(h_s+\eta-D\right)u\right)-\frac{\partial}{\partial y}\left(\left(h_s+\eta-D\right)v\right) \tag{3}$$

We will assume that before the start of wave generation, the speed and disturbance of the free surface were absent (4). The normal velocity component at the free boundary is calculated using the relation $u_n=c\eta/\left(H+\eta\right)$, and the boundary conditions of the "solid wall" are chosen in the form $u_n=0$. To solve Equations (2) and (3), the difference scheme of A. Sileski was used[29]. Pacific Ocean bathymetry with a resolution of 1 km was used for the simulation. Number of nodes of the numerical scheme 2720 x 12840 = 34924800. The generation of tsunami waves during the movement of a landslide and the propagation of a tsunami wave across the Pacific Ocean to an isobath of 10 meters were considered.

$$\eta(x, y, 0) = u(x, y, 0) = v(x, y, 0) = 0 \qquad (4)$$

6. Generation of a Tsunami Source from a Landslide Source

The estimated water area considered includes parts of the coasts of Chile and Peru, so most of the tide gauge records provide from Chile (**Figures 5**, **7**, **8**) are from these regions. The study analyzed four different scenarios for the formation of a tsunami source, each with varying initial characteristics of the landslide body. **Figure 20** shows eight time moments during the formation of the tsunami source for one of the scenarios. It is evident that at time t = 20 seconds (b), the wave front has a rounded shape, but starting at t = 30 seconds, the tsunami wave front extends in the direction of the landslide (c, d, e, f, g, h). The landslide comes to a stop at t = 100 seconds.

In Scenario 1, the landslide was modeled in two segments, with each block lifting over 30 seconds, and the maximum displacement reaching 15 meters. In Scenario 2, the landslide was modeled with 14 blocks. The blocks were lifted sequentially, each taking 10 seconds, and the maximum wave displacement reached 35 meters.

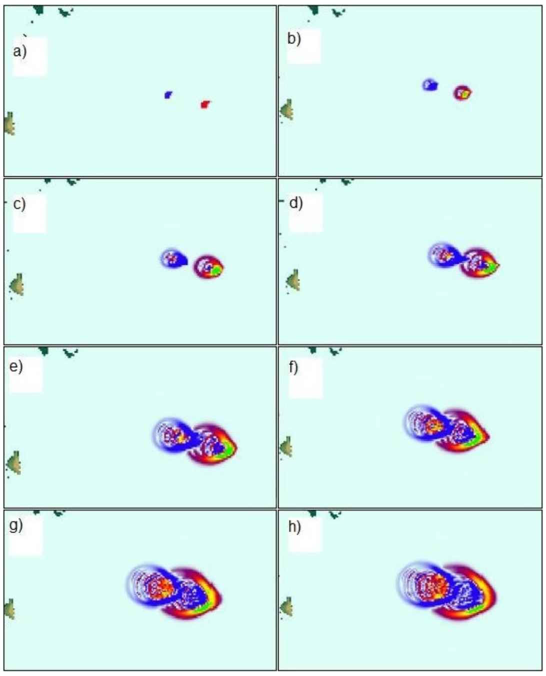

Figure 20. 8 time moments of tsunami source formation when a landslide moves down the volcano slope. **a**) t = 10 seconds; **b**) t = 20 seconds; **c**) t = 30 seconds; **d**) t = 40 seconds; **e**) t = 50 seconds; **f**) t = 60 seconds; **g**) t = 70 seconds; **h**) t = 80 seconds.

Figure 21 shows tsunami wave propagation over the design water area.

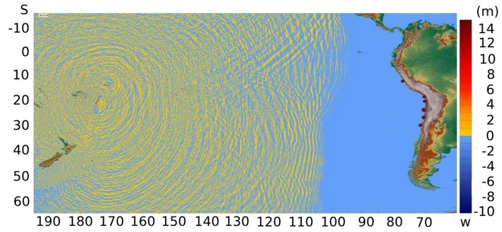

Figure 21. Tsunami wave propagation over the design water area 7 h 26 min after the end of the landslide process.

In Scenario 3, the landslide was modeled with 14 blocks. The blocks were lifted every 10 seconds, and the maximum wave displacement reached 25 meters. In Scenario 4, the landslide dimensions and number of blocks were the same as in Scenario 3. However, the characteristic times for movement of each block are differed. For block 1, it was 10 seconds; for block 2, 20 seconds; for block 3, 30 seconds; for block 4, 40 seconds; for block 5, 10 seconds; for block 6, 20 seconds; and for block 7, 30 seconds. The next seven blocks had symmetrical rise times. The maximum wave displacement for this scenario reached 35 meters.

Figure 22 illustrates the propagation of the tsunami wave over the computed water area 7 hours and 26 minutes after the sliding process concluded.

7. Wave Characteristics of a Tsunami from a Landslide Source along the Pacific Coastline

Figure 22 presents a histogram of wave heights along the coasts of Chile and Peru, as obtained from the Scenario 1 simulation. The maximum wave heights were recorded along the coast of Chile, between latitudes 24° and 25° S, reaching up to 0.8 meters. The average wave height for this scenario was 0.17 meters.

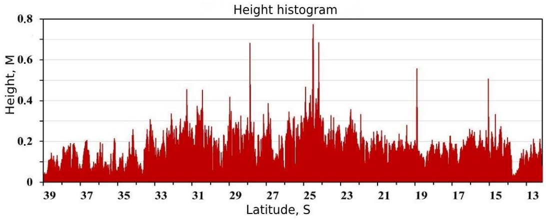

Figure 22. Histogram of the of maximum wave heights distribution along the coast of Chile and Peru in the simulation of Scenario 1.

For a more detailed analysis of the approach of the simulated waves, virtual tide gauges were set up according to the coordinates of real tidal stations in Chile and Peru. **Figure 23** shows records from virtual tide gauges during the simulation of Scenario 1.

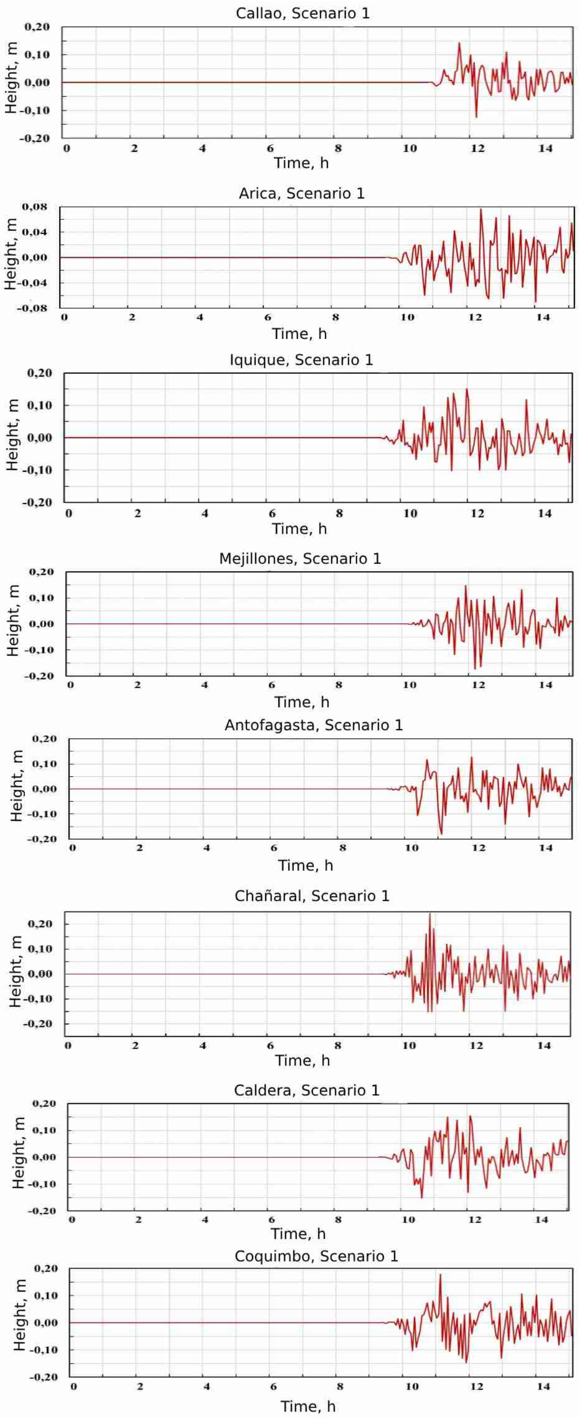
Callao, Scenario 1

Arica, Scenario 1

Iquique, Scenario 1

Mejillones, Scenario 1

Antofagasta, Scenario 1

Chañaral, Scenario 1

Caldera, Scenario 1

Coquimbo, Scenario 1

Figure 23. The records from virtual tide gauges obtained during the simulation of Scenario 1. The tide gauges are exposed in the locations: Peru - Callao, Chile - Arica, Iquique, Mejillones, Antofagasta, Chañaral, Caldera, Coquimbo.

- Callao station: the arrival time of the waves is 10 hours and 50 minutes after the volcanic eruption, with the maximum amplitude oscillations ranging from −0.13 to 0.15 meters.
- Arica station: the arrival time is 9 hours and 45 minutes, with amplitude oscillations ranging from −0.07 to 0.08 meters.
- Iquique station: the waves arrive at 9 hours and 20 minutes, with amplitude oscillations between −0.01 and 0.15 meters.
- Mejillones station: the arrival time is 9 hours and 45 minutes, with oscillations ranging from −0.17 to 0.15 meters.
- Antofagasta station: the waves arrive at 9 hours and 50 minutes, with oscillations between −0.19 and 0.14 meters.
- Chañaral station: the waves arrive at 9 hours and 30 minutes, with oscillations ranging from −0.15 to 0.23 meters.
- Caldera station: the arrival time is 9 hours and 30 minutes, with oscillations ranging from −0.15 to 0.15 meters.
- Coquimbo station: the arrival time is 9 hours and 40 minutes, with oscillations between −0.15 and 0.19 meters.

Figure 24 presents a histogram of wave heights along the coasts of Chile and Peru, obtained from the Scenario 2 simulation. The maximum wave heights were recorded along the coast of Chile, between latitudes 24° and 25° S, reaching 0.7 meters. The average wave height for this Scenario was 0.11 meters.

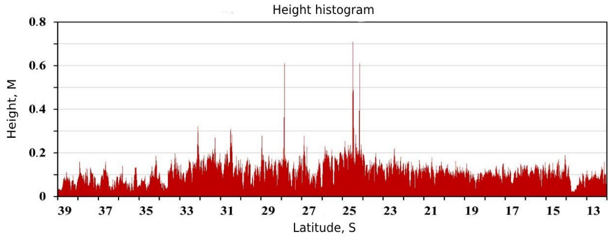
Height histogram

Figure 24. Histogram of the of maximum wave heights distribution along the coast of Chile and Peru in the simulation of Scenario 2.

For a more detailed analysis of the wave approach, **Figure 25** also includes records from virtual tide gauges during the Scenario 2 simulation:

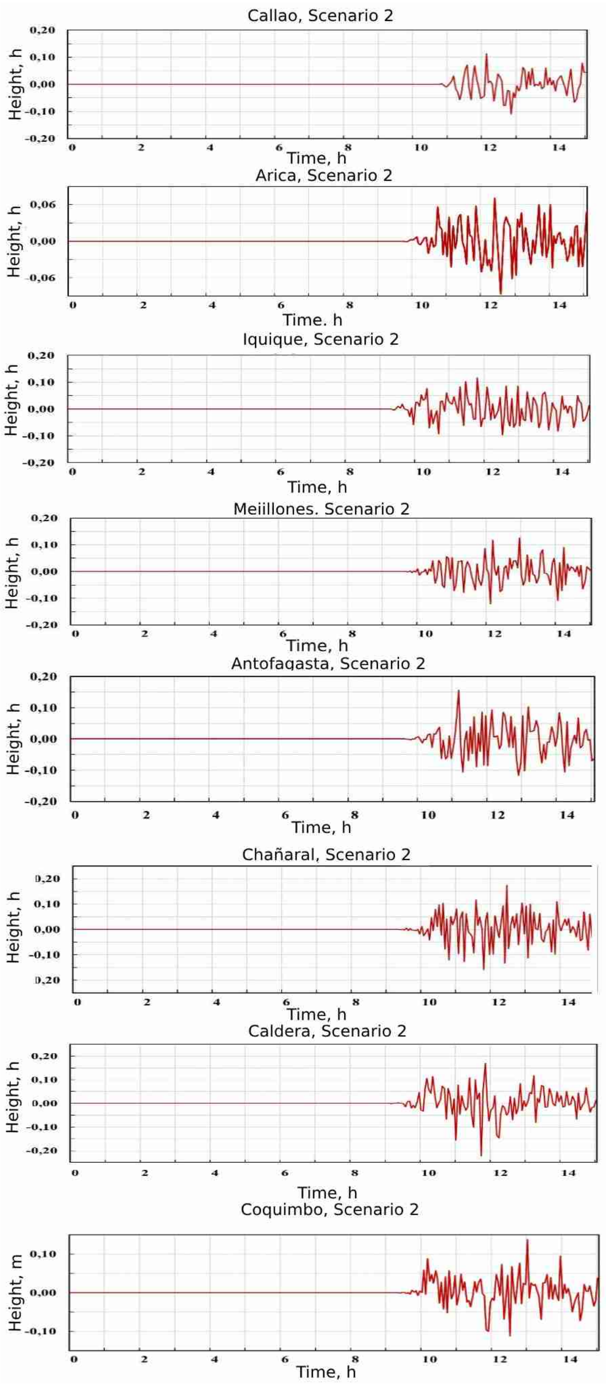

Figure 25. The records from virtual tide gauges obtained during the simulation of Scenario 2. The gauges are exposed in the locations of: Peru - Callao, Chile - Arica, Iquique, Mejillones, Antofagasta, Chañaral, Caldera, Coquimbo.

- Callao station: Wave arrival time is 10 hours and 50 minutes after the volcanic eruption. The maximum amplitude is in the range from −0.11 to 0.12 meters.
- Arica station: Wave arrival time is 9 hours and 45 minutes. The maximum amplitude is in the range from −0.07 to 0.07 meters.
- Iquique station: Wave arrival time is 9 hours and 20 minutes. The maximum amplitude spread ranges from −0.11 to 0.12 meters.
- Mejillones station: Wave arrival time is 9 hours and 45 minutes. The maximum amplitude is in the range from −0.12 to 0.14 meters.
- Antofagasta station: Wave arrival time is 9 hours and 50 minutes. The maximum amplitude is in the ranges from −0.12 to 0.16 meters.
- Chañaral station: Wave arrival time is 9 hours and 30 minutes, with a maximum in the range from −0.15 to 0.17 meters.
- Caldera station: Wave arrival time is 9 hours and 30 minutes. The maximum amplitude is in the range from −0.22 to 0.17 meters.
- Coquimbo station: Wave arrival time is 9 hours and 40 minutes. The maximum amplitude is in the range from −0.11 to 0.15 meters.

Figure 26 presents a histogram of wave heights along the coasts of Chile and Peru, obtained from the Scenario 2 simulation. The maximum wave heights were recorded along the coast of Chile, between latitudes 24° and 25° S, reaching 0.6 meters. The average wave height for this Scenario was 0.14 meters.

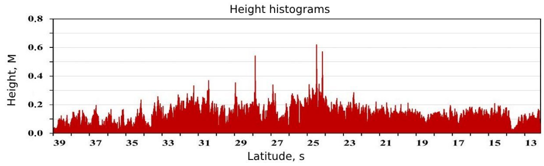

Figure 26. Histogram of the of maximum wave heights distribution along the coast of Chile and Peru in the simulation of Scenario 3.

For a more detailed analysis of the wave approach, **Figure 27** shows records from virtual tide gauges during the simulation of Scenario 3.

- Callao station: The arrival time of the waves is 10 hours and 50 minutes after the volcanic eruption. The maximum amplitude spread is from −0.11 to 0.9 meters.
- Arica station: The wave arrival time is 9 hours and 45 minutes. The maximum amplitude spread is from −0.08 to 0.07 meters.
- Iquique station: The wave arrival time is 9 hours and 20 minutes. The maximum amplitude range is from −0.09 to 0.11 meters.

- Mejillones station: The wave arrival time is 9 hours and 45 minutes. The maximum amplitude spread is from −0.12 to 0.15 meters.
- Antofagasta station: The wave arrival time is 9 hours and 50 minutes. The maximum amplitude range is from −0.12 to 0.11 meters.
- Chañaral station: The wave arrival time is 9 hours and 30 minutes. The maximum amplitude range is from −0.15 to 0.15 meters.
- Caldera station: The wave arrival time is 9 hours and 30 minutes. The maximum amplitude spread is from −0.17 to 0.10 meters.
- Coquimbo station: The wave arrival time is 9 hours and 40 minutes. The maximum amplitude range is from −0.15 to 0.08 meters.

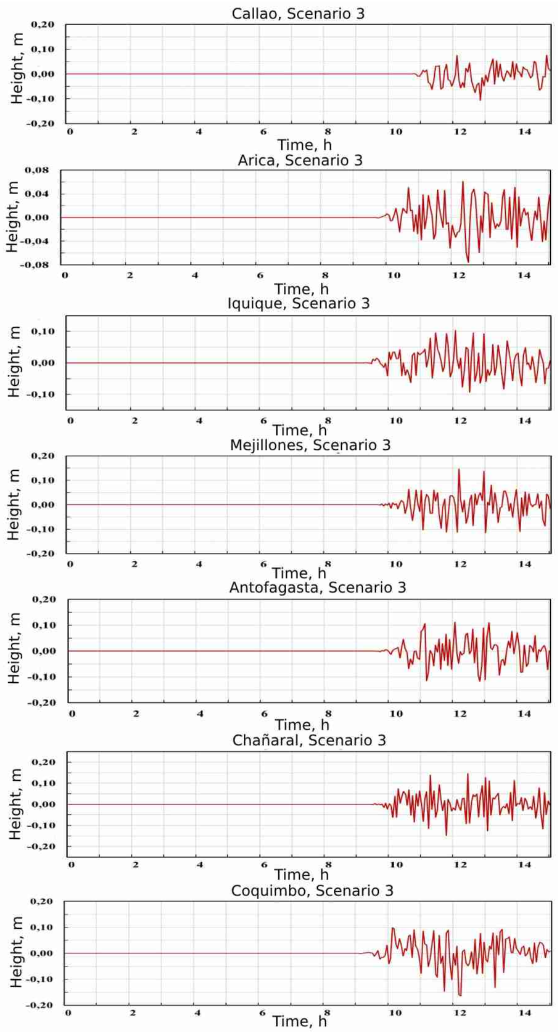

Figure 27. The records from virtual tide gauges obtained during the simulation of Scenario 3. The tide gauges are exposed in the locations of: Peru - Callao, Chile - Arica, Iquique, Mejillones, Antofagasta, Chañaral, Caldera, Coquimbo.

Figure 28 presents a histogram of wave heights along the coasts of Chile and Peru, obtained from the Scenario 2 simulation. The maximum wave heights were recorded along the coast of Chile, between latitudes 24° and 25° S, reaching 0.5 meters. The average wave height for this Scenario was 0.19 meters.

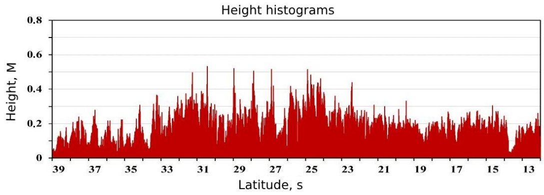

Figure 28. Histogram of the of maximum wave heights distribution along the coast of Chile and Peru in the simulation of Scenario 4.

For a more detailed analysis of the wave approach, **Figure 29** shows records from virtual tide gauges during the simulation of Scenario 4.

- Callao station: The arrival time of the waves is 10 hours and 50 minutes after the volcanic eruption. The maximum amplitude range is from −0.15 to 0.13 meters.
- Arica station: The wave arrival time is 9 hours and 45 minutes. The maximum amplitude spread is from −0.09 to 0.08 meters.
- Iquique station: The wave arrival time is 9 hours and 20 minutes. The maximum amplitude spread is from −0.12 to 0.13 meters.
- Mejillones station: The wave arrival time is 9 hours and 45 minutes. The maximum amplitude spread is from −0.16 to 0.20 meters.
- Antofagasta station: The wave arrival time is 9 hours and 50 minutes. The maximum amplitude range is from −0.14 to 0.18 meters.
- Chañaral station: The wave arrival time is 9 hours and 30 minutes. The maximum amplitude range is from −0.18 to 0.22 meters.
- Caldera station: The wave arrival time is 9 hours and 30 minutes. The maximum amplitude spread is from −0.24 to 0.17 meters.
- Coquimbo station: The wave arrival time is 9 hours and 40 minutes. The maximum amplitude range is from −0.18 to 0.15 meters.

To evaluate the modeling results, the computed tide gauge records were compared with field data. **Figures 30–38** present a comparison of field and calculated data for each Scenario. The comparison was made for the locations of Antofagasta, Chañaral, Coquimbo, and Arica, as these sites had the most noticeable wave displacements in the real records. **Figures 30** and **31** shows a comparison of field and computed records for Antofagasta (**Figure 30**). It is evident that the best agreement between the field and computed data was achieved in the modeling of Scenario 1.

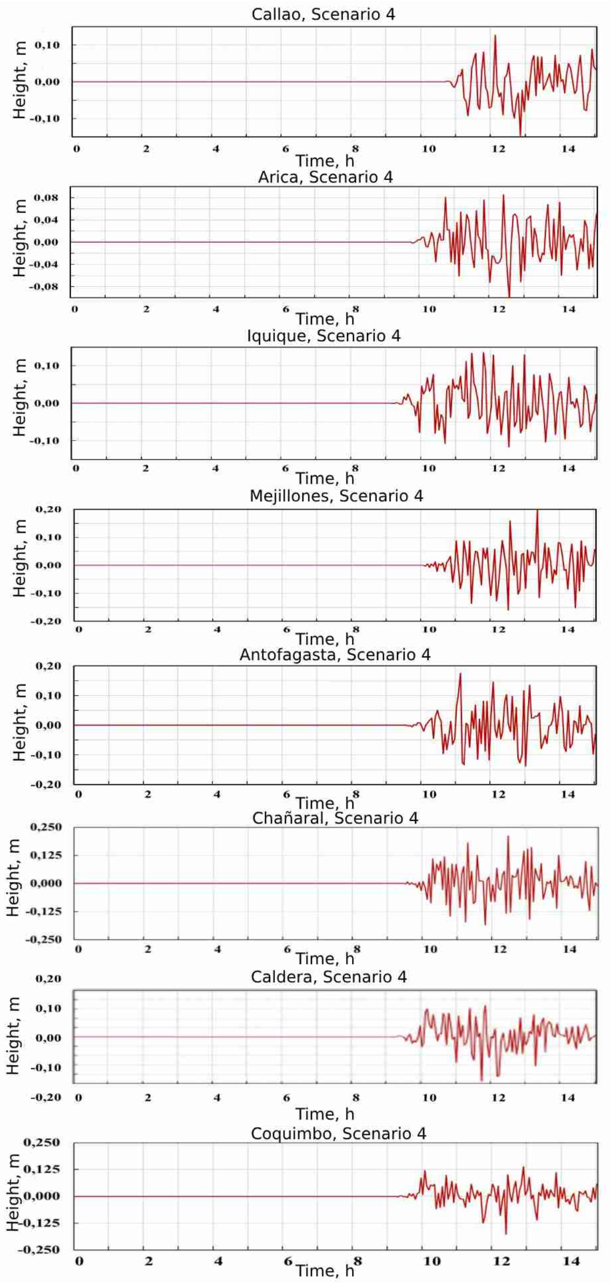

Figure 29. The records from virtual tide gauges obtained during the simulation of Scenario 4. The tide gauge stations are exposed in the locations of: Peru - Callao, Chile - Arica, Iquique, Mejillones, Antofagasta, Chañaral, Caldera, Coquimbo.

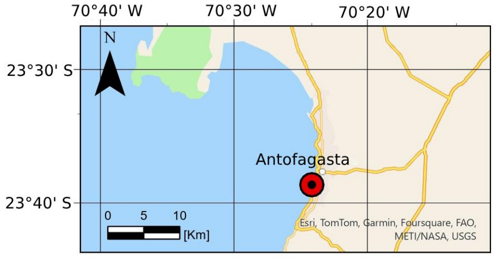

Figure 30. Location of Antofagasta on the coast of Chile. The point is marked with a red.

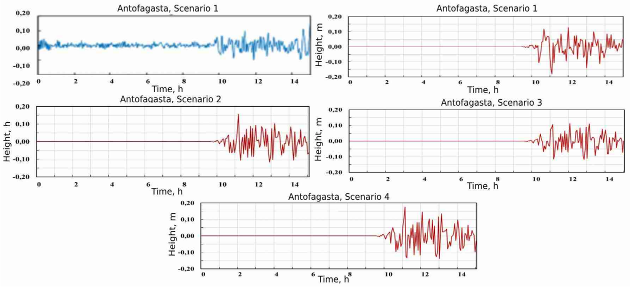

Figure 31. Comparison of observed and computed gauge diagrams for Antofagasta point.

Figures 32 and **33** presents a comparison of field and computed records for the Chañaral location It is evident that the best agreement between the field and computed data is achieved when modeling Scenario 4.

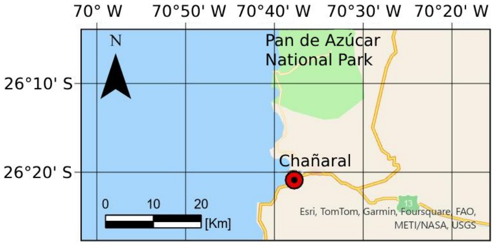

Figure 32. Location of Chañaral point on the coast of Chile. The point is marked with a red circle.

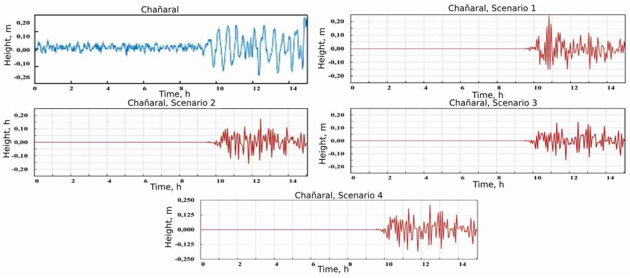

Figure 33. Comparison of observed and computed gauge diagrams for Chañaral point.

Figures 34 and **35** shows a comparison of field and computed records for the Coquimbo point. It is clearly seen that the best agreement between the field and computed data is obtained when modeling Scenario 4.

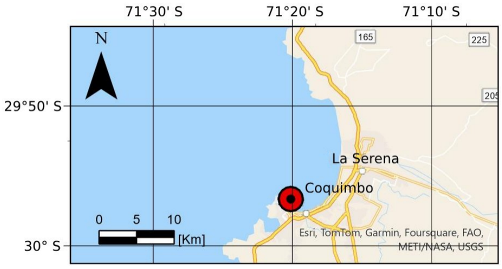

Figure 34. Location of point Coquimbo on the coast of Chile. The point is marked with a red circle.

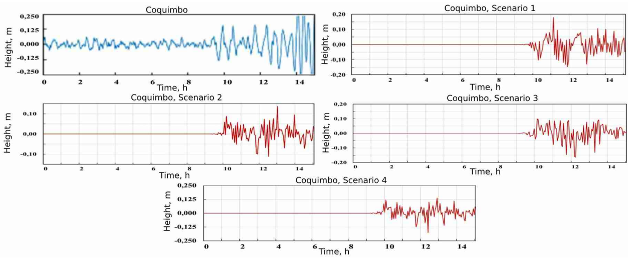

Figure 35. Comparison of observed and computed gauge diagrams for Coquimbo.

Figures 36 and **37** shows a comparison of field and calculated records for the Arica point. It is clearly seen that the best agreement between the field and calculated data is obtained when modeling Scenario 4.

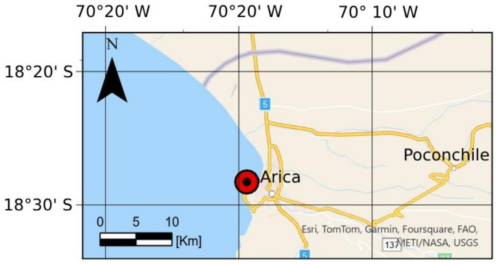

Figure 36. Location of point Arica on the coast of Chile. The point is marked in red circle.

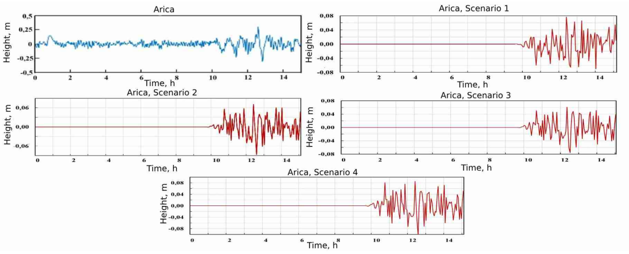

Figure 37. Comparison of observed and computed tide gauge diagrams for Arica Point does not give sufficient coincidence with the real records.

Figure 38 shows comparison of recordings from observed and virtual tide gauges for the following locations: Arica, Antofagasta, Coquimbo.

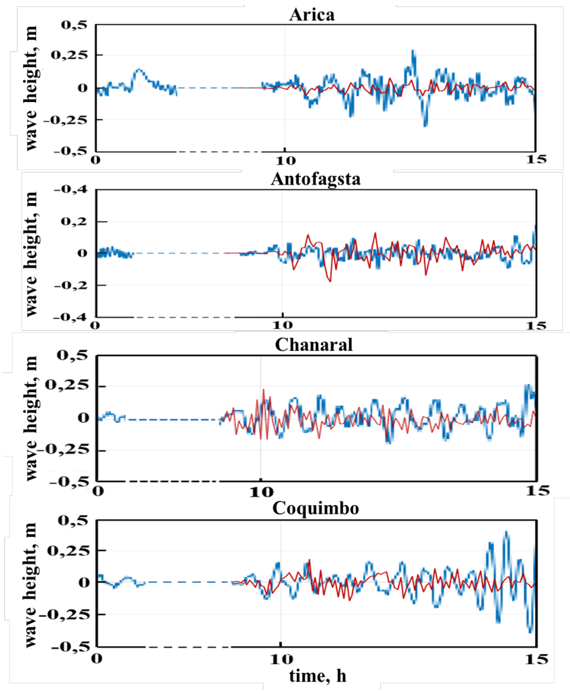

Figure 38. Comparison of recordings from real and virtual gauges for the following locations: Arica, Antofagasta, Coquimbo. The red line is the virtual recording, the blue line is the real recording. The dotted line marks the break in the record.

Table 3 also shows the maximum wave displacements recorded by field and calculated tide gauges. It is clearly seen that Scenario 4 gives the best result in terms of heights.

8. Conclusions

This paper proposes a mechanism for the appearance of ‘early’ tsunami waves on Chilean and Peru coasts of the Pacific Ocean, which arrived 4–5 hours earlier than the expected time of wave arrival at specific stations following the eruption of the Tonga volcano. Based on the observed data we hypothesize that a landslide, triggered by geodynamic stress during the eruption preparation in Tonga volcano, may have contributed in the early tsunami arrival. The study demonstrates that, in addition to the hypothesis found in the literature, which attributes this phenomenon to the generation of tsunami waves by Lamb waves, there is an alternative hypothesis: the early wave train could be generated by a pre-eruption landslide localized on the slope of the Tonga volcano.

Table 3. Comparison of the maximum and minimum displacements of field records and computed records for each scenario.

Point (Coordinates)	**Maximum Displacement, m**					**Minimum Displacement, m**				
	Natural Data	**Scenario**				**Natura Data**	**Scenario**			
		1	**2**	**3**	**4**		**1**	**2**	**3**	**4**
Callao (−12.07, −77.16)	0.19	0.16	0.15	0.12	0.18	−0.21	−0.16	−0.17	−0.14	−0.22
Arica (−18.47, −70.32)	0.3	0.09	0.09	0.10	0.11	−0.31	−0.09	−0.09	−0.09	−0.10
Iquique (−20.20, −70.14)	0.10	0.18	0.13	0.11	0.15	−0.09	−0.20	−0.13	−0.11	−0.15
Mejillones (23.09, −70.45)	0.21	0.24	0.17	0.16	0.24	−0.20	−0.21	−0.16	−0.15	−0.22
Antofagasta (−23.65, −70.40)	0.1	0.20	0.16	0.15	0.23	−0.1	−0.19	−0.18	−0.17	−0.23
Chañaral (−26.35, −70.63)	0.2	0.24	0.19	0.17	0.23	−0.19	−0.21	−0.17	−0.15	−0.21
Caldera (−27.06, −70.82)	0.09	0.21	0.23	0.20	0.27	−0.08	−0.20	−0.22	−0.19	−0.24
Coquimbo (−29.94, −71.33)	0.17	0.18	0.14	0.16	0.17	−0.19	−0.18	−0.15	−0.14	−0.18

As discussed in this work, the trigger for the landslide, which began with the accumulation of maximum stress, could have been either minor seismic forshocks (of which there were many prior to the eruption) or the process of preparing the volcanic eruption itself. The study characterizes the tsunami waves generated by a pre-eruption landslide process on a volcanic slope. The landslide was modeled as a rigid block segmented into multiple blocks. By considering different scenarios for the formation of a pre-eruption landslide source and analyzing the characteristics of the tsunami at specific stations, the possible timing of the underwater pre-eruption landslide prior to the eruption was estimated.

Assuming the proposed theory of tsunami wave generation by mass sliding is accurate, records from tide gauge stations worldwide suggest that submerged and semi-submerged volcanoes have the potential to trigger pre-eruption landslides, leading to tsunami waves that could reach coastal areas without warning. This presents a critical challenge for tsunami early warning systems, as we do not yet know how destructive these waves could be.

Author Contributions

Conceptualization, R.K.M., J.V.D.B.F. and A.K.; methodology, R.M., J.V.D.B.F. and A.K.; software, I.S.; validation, R.K.M., J.V.D.B.F. formal analysis, R.K.M., J.V.D.B.F., G.O.A.; investigation, R.K.M. and A.K.; resources, J.V.D.B.F. and A.K, data curation, R.K.M. and J.V.D.B.F.; writing—original draft preparation, I.S.and G.O.A.; writing—review and editing, R.K.M., A.K. and J.V.D.B.F.; visualization, I.S. and R.K.M.; supervision, R.K.M. and A.K.; project administration, R.K.M.; funding acquisition, A.K. and J.V.D.B.F.; All authors have read and agreed to the published version of the manuscript.

Funding

This research was funded by the Ministry of Science and Higher Education of the Russian Federation (agreement No. 075-15-2022-1127 dated July 1, 2022).

Institutional Review Board Statement

Not applicable.

Informed Consent Statement

Not applicable.

Data Availability Statement

The original contributions presented in the study are included in the article, further inquiries can be directed to the corresponding author

Conflicts of Interest

The authors declare no conflicts of interest.

References

[1] Nosov, A., Bolshakova, A.V., Sementsov, K.A., 2022. Energy characteristics of tsunami sources and the mechanism of wave generation by seismic movements of the ocean floor. Vestn. Moscow University Physics Bulletin. 76(S1), 136–142.

[2] Paris, R., 2015. Source mechanisms of volcanic tsunamis. Philosophical Transactions

of the Royal Society A. 373, 20140380. DOI: https://doi.org/10.1098/rsta.2014.0380

[3] Terry, J.P., Goff, J., Winspear, N., et al., 2022. Tonga volcanic eruption and tsunami, January 2022: globally the most significant opportunity to observe an explosive and tsunamigenic submarine eruption since AD 1883 Krakatau. Geoscience Letters. 9, 24. DOI: https://doi.org/10.1186/s40562-022-00232-z.

[4] Cronin, S., 2022. Tonga eruption likely the world's largest in 30 years – scientist: [Electronic resource]. rnz.co.nz – Radio New Zealand's information portal. Available from: https://www.rnz.co.nz/news/world/459657/tonga-eruption-likely-the-world-s-largest-in-30-years-scientist (cited 13 January 2023).

[5] Adushkin, V.V., Rybnov, Y.S., Spivak, A.A., 2022. Wave-related, electrical, and magnetic effects due to the January 15, 2022 catastrophic eruption of Hunga Tonga-Hunga Ha'aapai volcano. Journal of Volcanology and Seismology. 16, 251–263. DOI: https://doi.org/10.1134/S0742046322040029

[6] Heidarzadeh, M., Gusman, A.R., Ishibe, T., et al., 2022. Estimating the eruption-induced water displacement source of the 15 January 2022 Tonga volcanic tsunami from tsunami spectra and numerical modelling. Ocean Engineering. 261, 112165. DOI: https://doi.org/10.1016/j.oceaneng.2022.112165

[7] Lynett, P., McCann, M., Zhou, Z., et al., 2022. Diverse tsunamigenesis triggered by the Hunga Tonga-Hunga Ha'apai eruption. Nature. 609, 728–733. https://doi.org/10.1038/s41586-022-05170-6

[8] Omira, R., Ramalho, R.S., Kim, J., et al., 2022. Global Tonga tsunami explained by a fast-moving atmospheric source. Nature. 609, 734–740. DOI: https://doi.org/10.1038/s41586-022-04926-4.

[9] Cronin, S., 2022. Why the volcanic eruption in Tonga was so violent, and what to expect next: [Electronic resource]. theconversation.com – European news portal publishing news from the world of science. Available from: https://theconversation.com/why-the-volcanic-eruption-in-tonga-was-so-violent-and-what-to-expect-next-175035 (cited 22 March 2023).

[10] Molavi-Arabshahi, M., Arpe, K., 2022. Interactions between the Caspian Sea size (level) and atmospheric circulation. International Journal of Climatology. 42(16), 9626–9640.

[11] Hunga-Tonga-Hunga-Haapai eruption: [Electronic resource]. Available from: https://ru.wikipedia.org/wiki/ (cited 19 December 2022).

[12] Medvedev, I.P., Shepich, J., Fine, I.V., et al. Global tsunami caused by the eruption of Tonga volcano in January 2022. Physicochemistry of plant polymers: material from IV All-Russian scientific conference with international participation 'Tsunami waves: modelling, monitoring, forecasting'. Proceedings of the 70th anniversary of the catastrophic tsunami in Severo-Kurilsk; Moscow, Russia; 15–16 November 2022.

[13] Python programming language: [Electronic resource]. python.org – official high-level language site Python. Available from: https://www.python.org/ (cited 24 March 2022).

[14] Rara, destructiva y difícil de modelar: las características únicas de la erupción volcánica ocurrida en Tonga. Available from: https://uchile.cl/noticias/183755/las-caracteristicas-unicas-de-la-erupcion-volcanica-ocurrida-en-tonga (cited 26 January 2024).

[15] Sea Level Station, 2022. "Sea Level Monitoring Stations, Caldera, Coquimbo, Antofagasta, Mejillones, Iquiqu Ary 2022". UNESCO. Available from: https://www.ioc-selevelmonitoring.org/

[16] Iwasaki, S.I., 1997. The wave form and directivity of a tsunami generated by an earthquake and a landslide. Science of Tsunami Hazards. 15(1), 23–40.

[17] Watts, P., Imamura, F., Grilli, S., 2000. Comparing model simulations of three benchmark tsunami generation cases, Science of tsunami hazards. 18, 115–123.

[18] LeBlond, P.H., Jiang, L., 1991. The coupling between a submarine slide and the surface waves which it generates. Journal of Geophysical Research: Oceans. 97(C8), 12731–12744.

[19] Jiang, L., LeBlond, P.H., 1993. Numerical modelling of an underwater Bingham plastic mudslide and the waves which it generates. Journal of Geophysical Research: Oceans. 98(C6), 10303–10319.

[20] Kanamori, H., Kikuchi, M., 1993. The 1992 Nicaragua earthquake: a slow tsunami earthquake associated with subducted sediments. Nature. 361, 714–716.

[21] Ma, G., Kirby, J.T., Shi, F., 2013. Numerical simulation of tsunami waves generated by deformable submarine landslides. Ocean Modelling. 69, 146–165.

[22] Liu, W., He, S., 2016. A two-layer model for simulating landslide dam over mobile river beds. Landslides. 13, 565–576.

[23] Garagash, I.A., Lobkovsky, L.I., Kozyrev, O.R., et al., 2003. Generation and runup of tsunami waves at an submarine landslide. Oceanology. 43, 173–181.

[24] Lobkovsky, L.I., Mazova, R.K., Garagash, I.A., et al., 2006. Numerical simulation of generation of tsunami 7 February 1963 in Corinth Gulf, Greece. Russian Journal Of Earth Sciences. 8, ES5003. DOI: https://doi.org/10.2205/2006ES000210.2006

[25] Mazova, R.K., Kurkin, A.A., Okunev, D.A., 2022. Numerical modeling of a tsunami of landslide origin in the Kuril basin. Science of Tsunami Hazards. 41(4), 205–216.

[26] Lobkovsky, L., Mazova, R., Remizov, I., et al., 2021. Local tsunami run-up depending on initial localization of the landslide body at submarine slope. Landslides. 18, 897–907. DOI: https://doi.org/10.1007/

s10346-020-01489-1

[27] Papadopoulos, G.A., Lobkovsky, L.I., Mazova, R.K., et al., 2007. Numerical modeling of sediment mass sliding and tsunami generation: the case of 7 February 1963, in Corinth Gulf, Greece. Marine Geodesy. 30, 335–344.

[28] Volzinger, N.E., Klevaniy, K.A., Pelinovsky, E.N., 1989. Long-wave dynamics of the coastal zone. Gidrometeoizdat. 272p.

[29] Sielecki, A., Wurtele, M., 1970. The numerical integration of the non-linear shallow-water equations with sloping boundaries. Journal of Computational Physics. 6, 219–236.